Sami Ilvonen and Jukka Sarvas. 2007. Magnetic-field-induced ELF currents in a human body by the use of a GSM phone. IEEE Transactions on Electromagnetic Compatibility, volume 49, number 2, pages 294-301.

Magnetic-Field-Induced ELF Currents in a Human Body by the Use of a GSM Phone

Sami Ilvonen and Jukka Sarvas, *Member, IEEE*

***Abstract*—A finite element method (FEM) with nonuniform mesh is employed for the calculation of extremely low frequency (ELF) currents induced in a human body by a Global System for Mobile Communications (GSM) phone. The magnetic field of the phone is measured, and an equivalent source with magnetic dipoles is constructed for the numerical simulation. A cell of variable size is used in the simulation to accurately model the most important areas of the body model, namely areas close to the source and parts of the central nervous system. Three different mobile phone positions are considered: normal operation on the side of the head, breast pocket, and the small of the back where the spinal cord is close to the phone. Obtained results are compared with the guidelines of the International Commission on Non-Ionizing Radiation Protection (ICNIRP).**

***Index Terms*—Dosimetry, extremely low frequency (ELF), finite element method (FEM), Global System for Mobile Communications (GSM), International Commission on Non-Ionizing Radiation Protection (ICNIRP) guidelines, irregular mesh, mobile phone.**

I. Introduction

DURING operation, a Global System for Mobile Communications (GSM) phone sends data in short 15/26-ms packets [1]. As a consequence, the current flow from the battery to the transmitter is not constant, but varies according to the data packet structure of the GSM protocol. This pulsed battery current gives rise to a magnetic field around the phone. In a conducting material, like human tissues, this pulsed magnetic field induces currents. These currents have recently been studied [2], [3] in order to assess the exposure of the human head to the magnetic field. In earlier studies, other handheld appliances have also been considered. For example, in [4], currents induced by an electric shaver and hair dryers were calculated. In this paper, the exposure assessment calculations are extended with a more detailed head model and two new cases in which the phone is located in the breast pocket and on the small of the back where the spinal cord is closer to the phone.

As the pulse form of the mobile phone battery current is far from a sinusoidal signal, the newer statement of the International Commission on Non-Ionizing Radiation Protection (ICNIRP) [5] is better suited to study the exposure. For this weighted peak restriction assessment, the rate of change of magnetic flux density $\partial B/\partial t$ can be measured rather easily by using a coil. Since a mobile phone is a very compact source, the magnetic field induced by the phone decays rapidly as a function of distance. On the other hand, the phone is usually held very close to the body during operation. This means that in, order to properly predict the maximum induced current values, a more detailed model is required on areas close to the source.

In this study, the induced currents are computed using a finite element method (FEM) in the entire human body using the same measurement data as in [3] and with a realistic anatomical model with variable resolution. The model is individually adapted for each of the three considered mobile phone positions. The coarsest parts of the models that are farthest away from the source have a resolution of 8 mm. The parts close to the source have a resolution up to 1 mm. In the intermediate zone, there are parts with resolutions of 2 and 4 mm. This variable-sized meshing enabled us to calculate the maximum current densities with good accuracy using modest computational resources compared to the standard uniform mesh models. The obtained results are compared with the ICNIRP weighted peak restriction statement of the year 2003 [5].

II. Formulation

The fields due to the current pulses of the mobile phone battery can be considered quasi-static because the frequency spectrum of the pulses is in the range of 0.2–40 kHz, and in the human body, the conductivity σ and permittivity ϵ satisfy the condition $\sigma \gg 2\pi f\epsilon$. This also implies that the induced electric field $\mathbf{E}(\mathbf{r},t)$, with position vector $\mathbf{r}$ and time t, is directly due to the primary magnetic flux density $\mathbf{B}_0$ induced by the battery currents, as the first-order approximation. Therefore, the quasi-static Maxwell's equations of the form

$$\nabla \times \mathbf{E}(\mathbf{r},t) = -\frac{\partial \mathbf{B}_0(\mathbf{r},t)}{\partial t} \tag{1}$$

$$\nabla \times \mathbf{H}(\mathbf{r},t) = \mathbf{J}(\mathbf{r},t) \tag{2}$$

can be used, where $\mathbf{J}(\mathbf{r},t)$ is the current density and $\mathbf{H}(\mathbf{r},t)$ is the magnetic field. The primary magnetic flux density $\mathbf{B}_0$ can be represented using the vector potential $\mathbf{A}_0(\mathbf{r},t)$, $\mathbf{B}_0(\mathbf{r},t) = \nabla \times \mathbf{A}_0(\mathbf{r},t)$, and the electric field can be written with the scalar and vector potentials as

$$\mathbf{E}(\mathbf{r},t) = -\nabla\phi(\mathbf{r},t) - \frac{\partial \mathbf{A}_0(\mathbf{r},t)}{\partial t} \tag{3}$$

where $\phi(\mathbf{r},t)$ denotes the scalar potential. Due to the quasi-static approximation, the phase differences can be neglected and the time dependence can be separated as

$$\frac{\partial \mathbf{A}_0(\mathbf{r},t)}{\partial t} = \frac{\partial v(t)\mathbf{A}_0(\mathbf{r})}{\partial t} = v'(t)\mathbf{A}_0(\mathbf{r}) \tag{4}$$

Manuscript received November 18, 2005; revised May 9, 2006 and June 28, 2006. This work was supported by the National Technology Agency of Finland (TEKES), Filtronic LK Oy, Nokia Corporation, and the Graduate School of Telecommunication and Automation (GETA).

The authors are with the Electromagnetics Laboratory, Helsinki University of Technology, FI-02150 Espoo, Finland (e-mail: sami.ilvonen@tkk.fi; jukka.sarvas@tkk.fi).

Digital Object Identifier 10.1109/TEMC.2007.897145

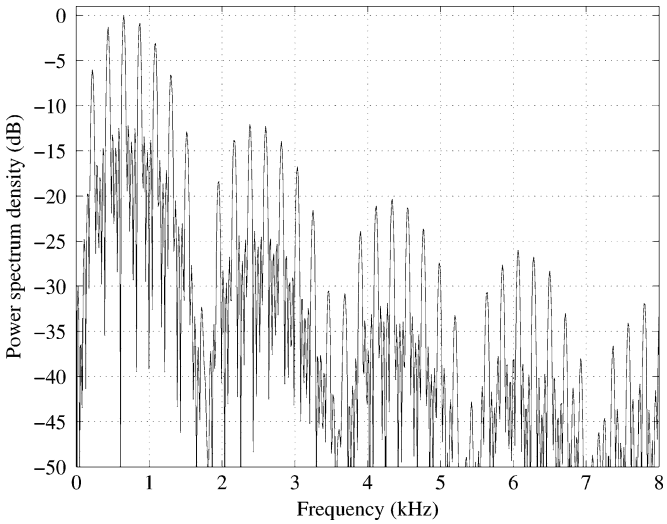

Fig. 1. Power spectrum density of the measured signal. This spectrum is not filtered using the low-pass filter of the ICNIPR statement [5].

where $v(t)$ is the time dependence and prime denotes time derivation.

Combining Ohm's law $\mathbf{J}(\mathbf{r}) = \sigma\mathbf{E}(\mathbf{r})$, condition $\nabla \cdot \mathbf{J}(\mathbf{r}) = 0$, and (3) with the boundary condition $\mathbf{n}(\mathbf{r}) \cdot \mathbf{J}(\mathbf{r}) = 0$ gives us an elliptic partial differential boundary value problem

$$\begin{cases} \nabla \cdot [\sigma(\mathbf{r})\nabla\phi(\mathbf{r}))] = -\nabla \cdot [\sigma(\mathbf{r})v'(t)\mathbf{A}_0(\mathbf{r})] \\ \mathbf{n}(\mathbf{r}) \cdot \nabla\phi(\mathbf{r}) = -\mathbf{n}(\mathbf{r}) \cdot v'(t)\mathbf{A}_0(\mathbf{r}). \end{cases} \tag{5}$$

After solving (5) for $\phi(\mathbf{r})$, the induced current can be computed as

$$\mathbf{J}(\mathbf{r}, t) = -\sigma(\mathbf{r})[\nabla\phi(\mathbf{r}) + v'(t)\mathbf{A}_0(\mathbf{r})]. \tag{6}$$

The value of the source vector potential $v'(t)\mathbf{A}_0(\mathbf{r})$ has to be determined from the measurements. Rate of change of magnetic flux density $v'(t)\mathbf{B}_0(\mathbf{r})$ is easy to measure as a voltage induced into a coil. However, determining the value of the vector potential $\mathbf{A}_0(\mathbf{r})$ from $\mathbf{B}_0(\mathbf{r})$ is complicated. One simple solution is to construct an equivalent source using the measurement data, and then, determine the vector potential from the parameters of the model. Details of this procedure are given in Section III.

III. Measurements and Equivalent Source

The measurement data used in this study are the same as in [3], where a GSM-type mobile phone was studied, and only a short description of the measurement procedure is given here. The measured phone gave the highest exposure values in [2], where seven different phone models were measured. The field $v'(t)\mathbf{B}_0(\mathbf{r})$ was measured in front of the mobile phone in a regular grid with a size of 210 mm × 150 mm and a resolution of 15 mm using a miniature dual coil with a volume of 2 cm^3. Seven similar layers were measured at different distances from the phone. The spectrum of the measured signal is shown in Fig. 1. A series of time pulses was recorded using a digital oscilloscope, and then, combined and averaged at each measurement point in order to reduce the noise. The obtained pulses were, then, filtered using a numerical low-pass filter according to the ICNIRP statement [5] in order to take into account the weighting of the frequency components above 1 kHz. As we were only interested in the maximum value of the induced current density, the value $\max_t |v'(t)||\mathbf{B}_0(\mathbf{r})|$ was determined from the measurements and used for the construction of the equivalent model.

The equivalent model was revised from the one presented in [3]. An equivalent current sheet that was used previously did not suit to cases where the source is close to a concave parts of the body, like the small of the back. There are several publications on the equivalent models for ELF exposure calculations [6]–[8], and most of these use a small current loop or a magnetic dipole as a source. From previous tests, it was already known that a single magnetic dipole did not give accurate enough results in the proximity of the phone. Better solution can be obtained using several dipoles, as shown in [8], where an arbitrary source is modeled using a group of dipoles arranged onto a cylindrical surface. This configuration does not fit into our problem, because the source is located very close to the body, and some dipoles would be too close or even inside the body. After some testing, the best results were obtained using an array of 28 magnetic dipoles arranged in a 7 × 4 grid with dimensions of 130 mm × 50 mm (approximately the dimensions of the phone). This grid was placed at a distance of 18 mm inward from the front of the phone, so that the field values of individual dipoles were not distinguishable on the front surface. The thickness of the phone in question was 2 cm, so the equivalent dipoles were located very close to the back of the phone.

Moments of these equivalent magnetic dipoles were fitted to the measurements by demanding that

$$\sum_{n=1}^{28} \nabla \left[\frac{v'(t)\mathbf{m}_n \cdot (\mathbf{r}_j - \mathbf{r}_n)}{4\pi|\mathbf{r}_j - \mathbf{r}_n|^3} \right] = v'(t)\mathbf{B}_0(\mathbf{r}_j) \tag{7}$$

where $\mathbf{m}_n$ and $\mathbf{r}_n$ are the moment and location of the nth magnetic dipole and $\mathbf{r}_j$ is the jth measurement point. The unknown moments $\mathbf{m}_n$ of (7) were determined using a regularized least-squares fitting. Maximum pointwise error of the obtained equivalent source was 4.5%. The source vector potential $v'(t)\mathbf{A}_0$ for the equation system (5) can now be easily constructed from the dipole moments as

$$v'(t)\mathbf{A}_0(\mathbf{r}) = \sum_{n=1}^{28} \frac{v'(t)\mathbf{m}_n \times (\mathbf{r} - \mathbf{r}_n)}{4\pi|\mathbf{r} - \mathbf{r}_n|^3}. \tag{8}$$

IV. Mesh Generator and Body Model

For the FEM field solver, we used a cubical element mesh with varying cube size. The straightforward approach to generate a finite element mesh with cubical elements of different sizes leads to an irregular mesh, i.e., mesh with nodes that are not correctly connected. Tetrahedral elements do not suffer from the same problem, and they are often used to model curved geometries. Robust and fast tetrahedral mesh generators are, however, very difficult to realize and the problem becomes very demanding when considering the complicated geometry of tissue boundaries in the human body. In this and the following sections, we present a combination of a mesh generator and an FEM solver

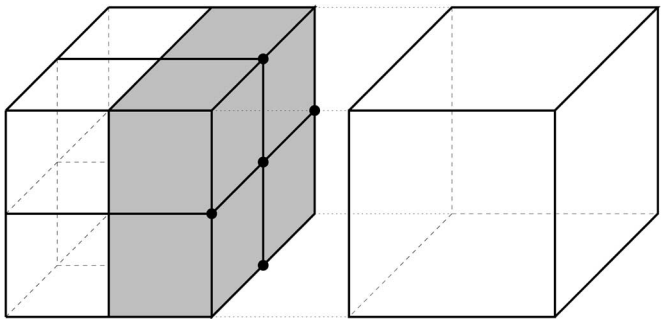

Fig. 2. Two adjacent elements shown with a slight separation. Five hanging nodes are denoted with circles; one of them is on the face and four on the edges. In order to force the continuity of the solution across the element boundary, values of the hanging nodes have to be constrained.

that can be efficiently used to solve the induced currents in a irregular cubical mesh.

From now on, we will call these incorrectly connected nodes in our irregular mesh as *hanging nodes*. An example of a mesh with two elements with five hanging nodes is given in Fig. 2. The problem with hanging nodes is that the solution is no longer continuous across the element boundaries as it should be. This problem can be removed by adding constraints to the finite element solver that force the continuity of the solution. A more detailed description of these techniques can be found in [9]. More details on the numerical solver used in this study are given in Section V.

The model of the human body was constructed using the data obtained from Brooks Air Force Laboratory [10]. This model is based on the data of the Visible Human Project [11] and has a resolution of 1 mm. Only some minor modifications were done to the Brooks model, like removing some nonconnected pixels that obviously did not belong to the body. The model consists of 38 tissues that are listed in Table I. The electrical properties, also obtained from Brooks Air Force Laboratory database, were modeled using the 4-Cole-Cole model presented in [12]. Although there is some variation on the conductivity values in the frequency range of 0.2–40 kHz, the values at the base frequency of 200 Hz were chosen for the simulation. This choice is justified by the frequency spectrum of the measured signal that showed that the main contribution of the pulses is concentrated on the lower frequencies. The obtained tissue conductivities are given in Table I.

For the mesh generator, three coarser models with resolutions of 2, 4, and 8 mm were constructed. The sizes are selected so that the coarsest mesh can be recursively refined by dividing a larger element into eight smaller ones. For each element in the coarser level, the tissue with largest volume inside the element was chosen according to the data of the finest model. Volumes of different tissues in all four models are given in Table I. In order to avoid removing fine structures of the central nervous system (CNS), all cells of coarser models that included even one 1-mm^3 cell of CNS tissues or CSF were marked so that one could restore the finer details of the structure when needed. Apart from these details, the mesh generator was constructed according to the principles presented in [9], although the practical details follow more closely to the ones given in [13], where very large hexahedral meshes are generated for earthquake simulations. One important aspect is the *2-to-1* requirement, which dictates that the size ratio between two elements connected to each other cannot be larger than 2. This requirement simplifies the construction of constraining equations for the FEM solver.

Three different computational meshes, one for each case, were, then, constructed using the mesh generator. The upper part of the mesh used for computing the currents in the head is shown in Fig. 3. One can see that the resolution of the mesh is dependent on the distance of the source so that spherical regions of different resolutions are formed. The CNS is modeled with the finest 1-mm resolution. In other cases, where the amount of CNS tissues close to the source is smaller, the available resourses were used to model the parts closer to the phone. Each of the final models had about 2.5 million elements and roughly the same number of nodes.

V. Numerical Solution Using FEM

The finite element solver of this study is based on the one used and tested in [3]. The solver used cubical elements with trilinear basis functions, and we have programmed it using PETSc library [14], [15] for data structures of sparse matrices and solvers. The correctness of the solver was tested by comparing it to analytical models of a layered sphere.

We had to do some modifications to the solver in order to implement the additional constraints required by the correct handling of the hanging nodes. When using trilinear basis functions, one can enforce the continuity of a mesh fulfilling the 2-to-1 requirement by two simple rules. First, one has to recognize the two different types of hanging nodes: 1) those that are on the edges of elements and 2) those that are in the middle of the face of an element. For a hanging edge node, one simply enforces constraint $\phi(\mathbf{r}_h) = 1/2[\phi(\mathbf{r}_a) + \phi(\mathbf{r}_b)]$, where $\phi(\mathbf{r}_h)$ is the scalar potential on the hanging node, and $\phi(\mathbf{r}_a)$ and $\phi(\mathbf{r}_b)$ are the potentials at the nodes at the ends of the edge of the hanging node. For the hanging face nodes, one has to enforce the condition $\phi(\mathbf{r}_h) = 1/4[\phi(\mathbf{r}_a) + \phi(\mathbf{r}_b) + \phi(\mathbf{r}_c) + \phi(\mathbf{r}_d)]$, where $\phi(\mathbf{r}_{a,b,c,d})$ are the potential values on the corners of the face on which the hanging node lies. These conditions have to be applied recursively, so that if some of the nodes a–d are hanging nodes, their values will eventually be calculated from a regular node. Applying these constraints to the system matrix will remove the unknowns of hanging edges and the continuity of the solution is forced.

When constructing the system matrix, (5) results in a symmetric positive definite system. This is a very desirable property, since it reduces memory consumption and is required for the convergence of the conjugate gradient method. So, in practice, one would like to add the constraints in a way that preserves the symmetry. As stated in [13], the constraints can be written in a form of a sparse matrix $\mathbf{B}$, so that the hanging nodes can be removed from the original system as follows:

$$\mathbf{u} = \mathbf{B}\tilde{\mathbf{u}} \tag{9}$$

where $\mathbf{B}$ is the constraints matrix, $\mathbf{u}$ is the vector of original unknown potential values at the nodes, and $\tilde{\mathbf{u}}$ is the vector of potential values with constraints applied. Now, the symmetry of

TABLE I
CONDUCTIVITIES AND VOLUMES OF DIFFERENT TISSUES IN THE FOUR MODELS USED BY THE MESH GENERATOR

Tissue	conductivity σ(S/m)	1 mm mesh volume (mm^3)	2 mm mesh volume (mm^3)	4 mm mesh volume (mm^3)	8 mm mesh volume (mm^3)
bile	1.40E+00	18991	18928	20160	23040
bladder	2.08E-01	103004	102536	99776	93696
blood	7.00E-01	640796	619680	643520	609280
blood vessel	3.07E-01	537085	496208	233792	56320
body fluid	1.50E+00	369213	350936	161088	91648
bone (cancellous)	8.15E-02	1686965	1702608	1654848	1015296
bone (cortical)	2.02E-02	2412881	2412768	2214912	1178624
bone marrow	2.27E-03	2806039	2789584	2881664	3460096
cartilage	1.74E-01	509334	503096	494592	424448
cerebellum*	1.19E-01	128874	130512	139392	155648
cerebral spinal fluid	2.00E+00	211766	192920	178752	216576
eye (aqueous humor)	1.50E+00	11822	12008	13184	13824
eye (cornea)	4.23E-01	239	312	0	0
eye (lens)	3.27E-01	898	832	896	1024
eye (sclera/wall)	5.05E-01	3320	3000	640	0
fat	2.24E-02	33374895	33220472	33359552	34363904
gall bladder	9.00E-01	10381	10504	7744	1536
glands	5.24E-01	142193	142880	140864	138240
gray matter*	9.88E-02	524933	529200	597184	620544
heart	1.06E-01	306063	306552	302336	290304
intestine (large)	2.32E-01	455205	471592	479744	159232
intestine (small)	2.32E-01	781639	795496	827968	687616
kidneys	1.13E-01	336388	339128	345728	354816
ligaments	1.74E-01	2464170	2444480	2114560	1595392
liver	4.14E-02	1789268	1800544	1835648	1936896
lung	7.95E-02	3407473	3419928	3562432	3689472
lymph	5.24E-01	63164	55392	40448	24064
muscle	3.21E-01	42815296	43057728	44057152	45943296
mucous membrane	6.57E-04	460314	405040	171712	127488
nails (toe & finger)	2.02E-02	3115	2728	512	0
nerve (spine)*	2.88E-02	347712	337224	307584	220160
pancreas	5.24E-01	84857	84064	86656	88064
skin / dermis	2.00E-04	4873994	4859376	3859136	706048
spleen	1.03E-01	241552	241128	244544	268288
stomach	5.24E-01	150526	154728	160384	120832
testicles	4.24E-01	21731	21472	24384	33792
tooth	2.02E-02	13198	13024	17344	22528
white matter*	6.26E-02	447684	451368	471040	539136

Tissues marked with an asterisk (*) are categorized as central nervous system.

the original equation system $\mathbf{Au} = \mathbf{b}$ can be preserved using matrix $\mathbf{B}$ as

$$\mathbf{B}^T\mathbf{AB}\tilde{\mathbf{u}} = \mathbf{B}^T\mathbf{b}. \tag{10}$$

In practice, this can be done efficiently during the matrix assembly, since the sparse matrix–matrix products are time-consuming.

The correctness of the new program was tested with several different models, where first the uniform mesh, and then, the mesh with hanging nodes were computed. Also, the original layered sphere models were again compared to the new solver code. For the results presented in this paper, a conjugate gradient solver with incomplete Cholesky preconditioner was used.

VI. RESULTS

A. Averaging

In order to compare the results with the ICNIRP guidelines, the current densities have to be averaged over a 1-cm^2 area normal to their direction. For the averaging process, the obtained solutions were transformed back from the FEM mesh into a Cartesian cubical mesh with a resolution of 1 mm. For each Cartesian component, the mesh was divided into layers 1 mm

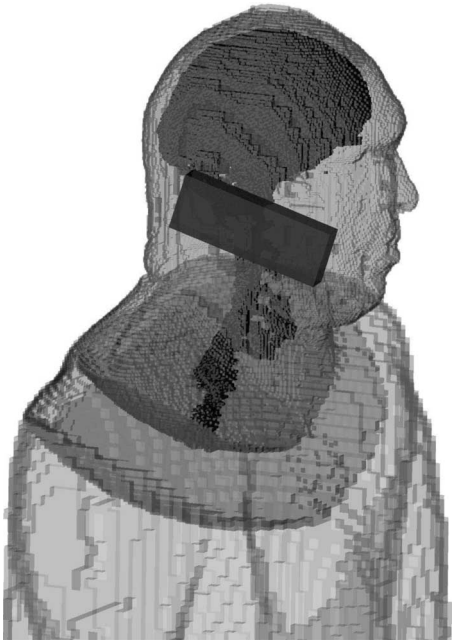

Fig. 3. Mesh used for the head and the position of the mobile phone.

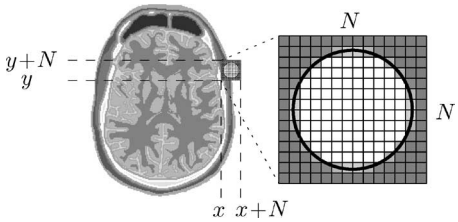

Fig. 4. Averaging process. The resolution of the grid is 1 mm, and the area of the circle is 1 cm^2.

apart and normal to the direction of the current component. The current densities on these layers were, then, averaged using a weighted sum, e.g., for the J_z-components on the layer z_n

$$J_{z\,\mathrm{avg}}\left(x+\frac{N}{2}, y+\frac{N}{2}, z_n\right) = \sum_{i=1}^{N}\sum_{j=1}^{N} w(i,j) J_z(x+i, y+j, z_n)$$

where $w(i,j)$ denotes the weight, N is the size of the weight array, and x and y are the coordinates on the layer z_n (see Fig. 4). The values of the weights were chosen so that the effective area corresponds to a circle with an area of 1 cm^2 and $\sum_{i,j} w(i,j) = 1$.

This process was repeated for each layer and Cartesian component. The total averaged current density was calculated using the averaged Cartesian current components as $J_{\mathrm{tot}} = \sqrt{J^2_{x\,\mathrm{avg}} + J^2_{y\,\mathrm{avg}} + J^2_{z\,\mathrm{avg}}}$ for each point of the 1-mm grid. In practice, the aforementioned averaging is often used in digital image processing, and is easy and efficient to implement using two-dimensional convolution and fast Fourier transformation. For details, see [16].

TABLE II
MAXIMUM VALUES OF AVERAGED CURRENT DENSITIES

Phone position	Current density (μA/m^2)
Cheek	83
Breast pocket	45
Small of the back	28

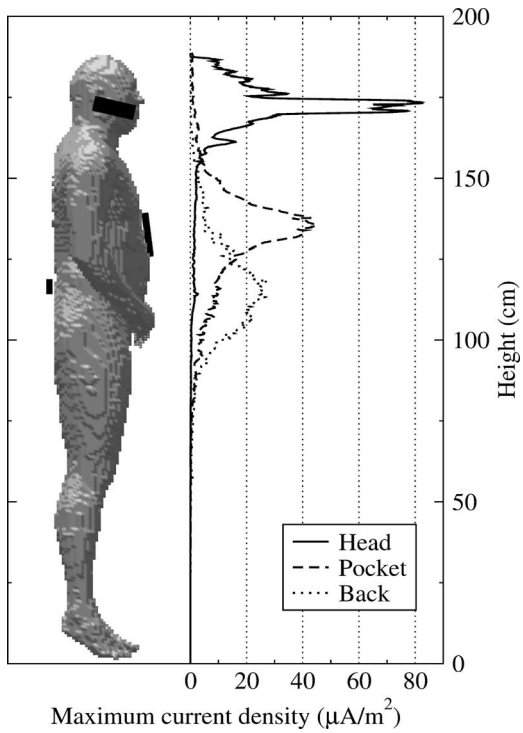

Fig. 5. Maximum values of averaged current densities per transaxial layer.

B. Obtained Maximum Values

The obtained maximum values of the averaged current densities for each phone position are given in Table II. Fig. 5 shows the maximum value per transaxial plane for each solution. As seen from this graph, the current densities drop rather quickly when moving away from the source, especially in the case when the phone is held by the ear. The corresponding transaxial planes from the locations of the maximas of the graphs are shown in Figs. 6–8. The largest obtained averaged current density value in the CNS was 35 $\mu A/\mathrm{m}^2$.

C. Position of the Phone

Since the source is located very close to the body, the obtained current densities are strongly dependent on the distance between the body model and the source. Several simulations with small variations in the source position were made to get an estimate of the stability of the setup.

First, the effect of the distance was tested by positioning the phone to a normal operating position shown in Fig. 3. Three simulations were made using 0, 5, and 10 mm distance between

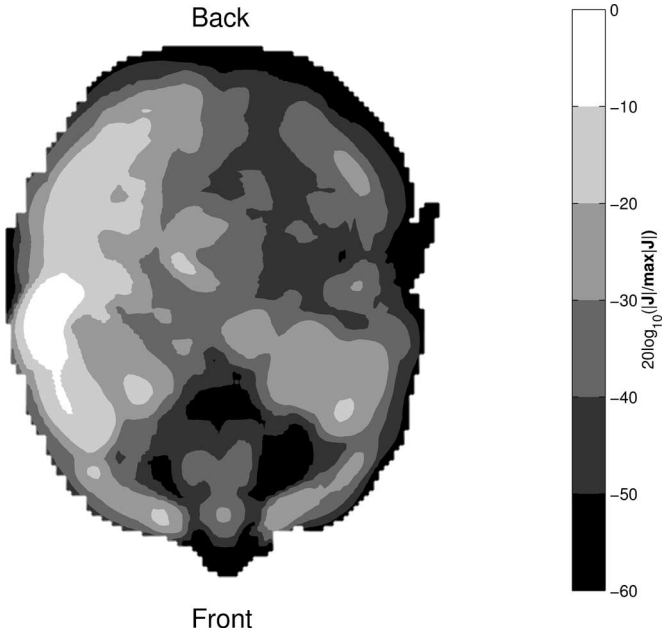

Fig. 6. Averaged current densities on a transaxial plane at the location of the maximum when the phone is located close to the ear. Averaged current density is shown as a decibel value compared to the maximum value (e.g., $20\ \log_{10}(|\mathbf{J}|/\max|\mathbf{J}|)$).

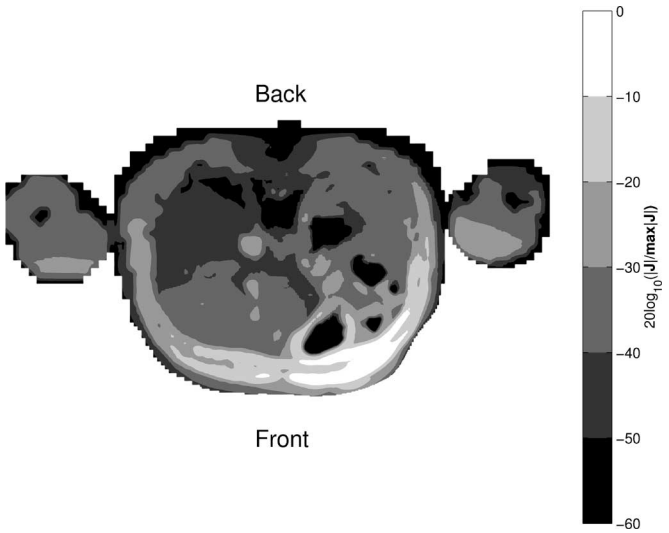

Fig. 7. Averaged current densities on a transaxial plane at the location of the maximum when phone is located in the breast pocket. Averaged current density is shown as a decibel value compared to the maximum value (e.g., $20\ \log_{10}(|\mathbf{J}|/\max|\mathbf{J}|)$).

the phone and the body model. The obtained current densities were averaged according to the method given in Section VI-A with all tissues taken into account. Another test was made for the breast pocket case. The results are given in Table III. The effect of the position of the phone on the cheek was also tested by moving the phone slightly in an up–down direction, but the change in results (for both CNS and other tissues) was small compared to the variation in distance.

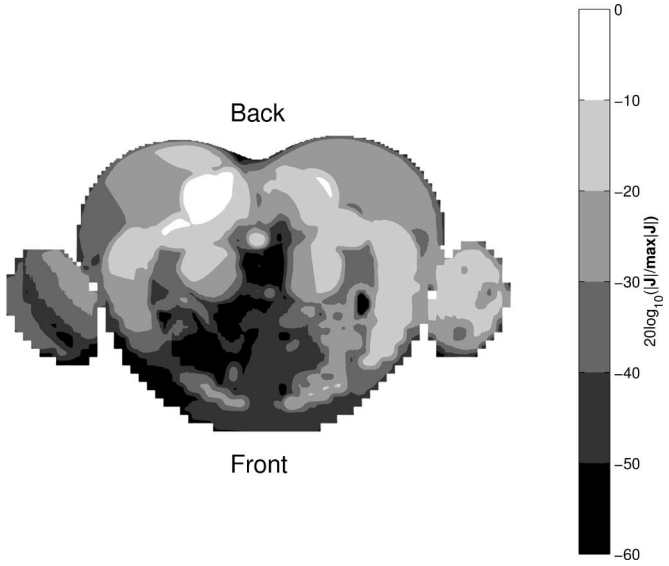

Fig. 8. Averaged current densities on a transaxial plane at the location of the maximum when the phone is located at the small of the back. Averaged current density is shown as a decibel value compared to the maximum value (e.g., $20\ \log_{10}(|\mathbf{J}|/\max|\mathbf{J}|)$).

TABLE III
EFFECT OF THE DISTANCE BETWEEN THE SOURCE AND THE BODY MODEL

Distance (mm)	Current density (μA/m^2)
from cheek	
0	83
5	63
10	49
from chest	
0	45
5	36
10	30

D. Effect of the Resolution of the Body Model

The effect of the resolution of the mesh was examined by using different refinement levels of the body model. Since the largest obtained values were observed when the phone was held on the cheek, the tests were done using that configuration. The results were calculated for four different meshes starting from the coarsest uniform mesh with a constant resolution of 8 mm. The successive meshes were, then, generated by refining the previous mesh, until the resolution of the finest part was 1 mm. The locations of the highest values were inspected so that the largest peak value was always inside the refined volume.

Table IV lists the maximum averaged current densities obtained using different mesh resolutions. It can be seen that the highest value was obtained when the resolution was 2 mm. Refining the mesh to the resolution of 1 mm did not give larger

TABLE IV
MAXIMUM AVERAGED CURRENT DENSITIES OBTAINED USING DIFFERENT MESH RESOLUTIONS

Minimum cell size (mm)	8	4	2	1
Current density (μA/m^2)	67	74	83	80

TABLE V
RELATIVE MAXIMUM VALUES OF THE NONAVERAGED INDUCED CURRENT DENSITY WITH DIFFERENT MESH RESOLUTIONS

Minimum cell size (mm)	8	4	2	1
Percent of obtained maximum	30 %	40 %	82 %	100 %

values. However, the nonaveraged maximum current densities showed stronger dependence on the mesh resolution, as can be seen from Table V, where the relative maximum values are given (largest value was obtained using 1-mm resolution, and other values are normalized with this maximum). A more detailed study showed that the maximum averaged value was induced in the parotid gland situated right beneath the phone, whereas the peak value was obtained in the fine layer of cerebrospinal fluid between the brain tissue and the skull.

VII. DISCUSSION

A previous study [3] gave the maximum averaged current density of 72 $\mu A/\mathrm{m}^2$ for the FEM solver and 80 $\mu A/\mathrm{m}^2$ for the finite integration technique (FIT) solver for a single Cartesian component. The "worst-case" value for the total current density, calculated by using the maximum values for each Cartesian component and combining these into a same point, was 101 $\mu A/\mathrm{m}^2$ when using the FEM solver and 115 $\mu A/\mathrm{m}^2$ for the FIT solver with lower resolution. In this study, the comparable configuration is the one where a user is holding the phone close to the ear. Since the previous results were calculated with a model that consisted only of the CNS, the comparable value is the obtained maximum current density of 35 $\mu A/\mathrm{m}^2$. This value is in line with the result obtained before, considering the following.

1) The exact positioning of the phone is different. As the tests in Section VI-C show, the position has a large effect on the current density.
2) A different anatomical model is used, which also affects the distance between the phone and CNS.

From Figs. 5–8, one can see that the current drops rather rapidly when moving away from the source. This justifies our use of different element sizes in a mesh that is refined according to the closeness of the source and tissue type. In particular, the effect of tissue conductivity is seen in Fig. 8, where the maximum current is induced rather deep in the back muscles. This is due to the much lower conductivity of the fat tissue compared to the muscle. In the same figure, the spinal cord is also observable, and this is the main advantage of the nonuniform mesh approach: important tissues can be studied with any accuracy even when buried deeper inside the body.

As stated in earlier studies also [4], the distance between the source and the body has a strong effect on the results when considering small handheld appliances. In our case, the phone is held in contact (without galvanic coupling) with the body, so the equivalent model and the geometrical configuration of the source are critical, as the tests show.

The effect of the model resolution was tested in Section VI-D. Even though the better resolution gives higher peak values to areas with thin highly conductive parts, the averaging over the 1-cm^2 area effectively levels off the peak values of the finer model. All obtained values were rather small when compared to the ICNIRP basic restriction rule [5], which is $2\sqrt{2}$ mA/m^2.

VIII. CONCLUSION

The FEM with irregular cubical mesh and hanging nodes was used to evaluate the magnetic field induced currents in three different cases of GSM-type mobile phone usage. Several tests were made to examine the uncertainties due to the method used and geometrical variation on phone positions. The results obtained are considerably lower than the basic restriction limit given in the ICNIRP guidelines. This further qualifies the previously obtained results. The suitability of the locally refined models for calculating the induced currents from small appliances held close to the body was also discussed. The use of refinements enables the use of very detailed models with moderate computational resources.

ACKNOWLEDGMENT

The authors would like to thank S. Järvenpää from the Helsinki University of Technology for his help in testing and developing the FEM solver, and A.-P. Sihvonen and A. Turunen from STUK—Finnish Radiation and Nuclear Safety Authority—for the measurement data, and Brooks Airforce Base for providing the human model.

REFERENCES

[1] A. Mehrotra, *GSM System Engineering*. Norwood, MA: Artech House, 1997.
[2] K. Jokela, L. Puranen, and A.-P. Sihvonen, "Assessment of the magnetic field exposure due to the battery current of digital mobile phones," *Health Phys.*, vol. 86, no. 1, pp. 56–66, 2004.
[3] S. Ilvonen, A.-P. Sihvonen, K. Kärkkäinen, and J. Sarvas, "Numerical assessment of induced ELF currents in the human head due to the battery current of a digital mobile phone," *Bioelectromagnetics*, vol. 26, no. 8, pp. 648–656, 2005.
[4] J. Cheng, M. A. Stuchly, C. DeWagter, and L. Martens, "Magnetic field induced currents in a human head from use of portable appliances," *Phys. Med. Biol.*, vol. 40, pp. 495–510, 1995.
[5] The International Comission on Non-Ionizing Radiation Protection (ICNIRP), "Guidance on determining compliance of exposure to pulsed and complex non-sinusoidal waveforms below 100 kHz with ICNIRP guidelines," *Health Phys.*, vol. 84, no. 3, pp. 383–387, Mar. 2003.
[6] L. E. Zaffanella, T. P. Sullivan, and I. Visintainer, "Magnetic field characterization of electrical appliances as point sources through in situ measurements," *IEEE Trans. Power Del.*, vol. 12, no. 1, pp. 443–450, Jan. 1997.
[7] K. Yamazaki and T. Kawamoto, "Simple estimation of equivalent magnetic dipole moment to characterize ELF magnetic fields generated by electric appliances incorporating harmonics," *IEEE Trans. Electromagn. Compat.*, vol. 43, no. 2, pp. 240–245, May 2001.

[8] S. Nishizawa, H.-O. Ruoß, F. M. Landstorfer, and O. Hashimoto, "Numerical study on an equivalent source model for inhomogeneous magnetic field dosimetry in the low-frequency range," *IEEE Trans. Biomed. Eng.*, vol. 51, no. 4, pp. 612–616, Apr. 2004.
[9] P. Schimpf, D. Haynor, and Y. Kim, "Object-free adaptive meshing in highly heterogeneous 3-D domains," *Int. J. Bio-Med. Comput.*, vol. 40, pp. 209–225, 1996.
[10] Brooks Air Force Laboratory. (2005, Jun.). [Online]. Available: http://www.brooks.af.mil/AFRL/HED/hedr/hedr.html
[11] U.S. National Institute of Health, National Library of Medicine. (2005, Jun.). [Online]. Available: http://www.nlm.nih.gov/research/visible/index.html
[12] C. Gabriel and S. Gabriel, "Compilation of dielectric properties of body tissues at RF and microwave frequencies," Armstrong Laboratory (AFMC), Radio Frequency Radiation Div., Brooks AFB, San Antonio, TX, Tech. Rep. AL/OE-TR-1996-0037, 1996.
[13] V. Akçelik, J. Bielak, G. Biros, I. Epanomeritakis, A. Fernández, O. Ghattas, E. J. Kim, J. López, D. O'Hallaron, T. Tu, and J. Urbanic, "High resolution forward and inverse earthquake modeling on terasacale computers," presented at the SC 2003, Phoenix, AZ, Nov. 2003.
[14] S. Balay, K. Buschelman, W. D. Gropp, D. Kaushik, M. Knepley, L. C. McInnes, B. F. Smith, and H. Zhang. (2001). PETSc home page [Online]. Available: http://www.mcs.anl.gov/petsc
[15] S. Balay, K. Buschelman, W. D. Gropp, D. Kaushik, M. Knepley, L. C. McInnes, B. F. Smith, and H. Zhang, "PETSc users manual," Argonne Nat. Lab., Argonne, IL, Tech. Rep. ANL-95/11, Revision 2.1.5, 2004.
[16] W. K. Pratt, *Digital Image Processing*, 3rd ed. New York: Wiley, 2001, Ch. 7.

Sami Ilvonen was born in Juuka, Finland, in 1975. He received the M.Sc. degree in electrical engineering in 2000 from the Helsinki University of Technology, Espoo, Finland, where he is currently working toward the D.Sc. degree at the Electromagnetics Laboratory.

His current research interests include electromagnetic field computing and bioelectromagnetics.

Jukka Sarvas (A'99–M'98) received the M.Sc. and Ph.D. degrees in mathematics from the University of Helsinki, Helsinki, Finland, in 1968 and 1972, respectively.

During 1982–1984, he was with Outokumpu Company. From 1988 to 2002, he was the Director of the Rolf Nevanlinna Research Institute of Applied Mathematics and Statistics, University of Helsinki, where he was a Visiting Researcher during 1974–1975. He has also been a Visiting Researcher at the University of Michigan during 1979–1980, and at the University of Illinois at Urbana-Champaign during 1999–2000, 2003, and 2005. Since 2002, he has been a Professor of computational electromagnetics in the Electromagnetics Laboratory, Helsinki University of Technology, Espoo, Finland. His current research interests include electromagnetic field computing, in particular, with integral equations and fast methods.